Critical Decay Index at the Onset of Solar Eruptions

Francesco Zuccarello, Guillaume Aulanier, Stuart Gilchrist

CRITICAL DECAY INDEX AT THE ONSET OF SOLAR ERUPTIONS

F. P. Zuccarello, G. Aulanier, and S. A. Gilchrist
LESIA, Observatoire de Paris, PSL Research University, CNRS, Sorbonne Universités, UPMC Univ. Paris 06, Univ. Paris Diderot, Sorbonne Paris Cité, 5 place Jules Janssen, F-92195 Meudon, France; Francesco.Zuccarello@obspm.fr, Guillaume.Aulanier@obspm.fr, Stuart.Gilchrist@obspm.fr

ABSTRACT

Magnetic flux ropes are topological structures consisting of twisted magnetic field lines that globally wrap around an axis. The torus instability model predicts that a magnetic flux rope of major radius R undergoes an eruption when its axis reaches a location where the decay index $-d\,(\ln B_{\mathrm{ex}})/d\,(\ln R)$ of the ambient magnetic field B_{ex} is larger than a critical value. In the current-wire model, the critical value depends on the thickness and time evolution of the current channel. We use magnetohydrodynamic simulations to investigate whether the critical value of the decay index at the onset of the eruption is affected by the magnetic flux rope's internal current profile and/or by the particular pre-eruptive photospheric dynamics. The evolution of an asymmetric, bipolar active region is driven by applying different classes of photospheric motions. We find that the critical value of the decay index at the onset of the eruption is not significantly affected by either the pre-eruptive photospheric evolution of the active region or the resulting different magnetic flux ropes. As in the case of the current-wire model, we find that there is a "critical range" [1.3–1.5], rather than a "critical value" for the onset of the torus instability. This range is in good agreement with the predictions of the current-wire model, despite the inclusion of line-tying effects and the occurrence of tether-cutting magnetic reconnection.

Key words: instabilities – magnetohydrodynamics (MHD) – methods: numerical –
Sun: coronal mass ejections (CMEs)

1. INTRODUCTION

Solar eruptions are one of the most spectacular and violent phenomena that occur in the Sun's atmosphere. Together with solar flares, they are the most impulsive and energetic manifestation of solar activity. Energy considerations suggest that eruptions, as well as the associated coronal mass ejections (CMEs), are magnetically driven (Forbes et al. 2006).

A significant number of eruptions originate in active regions where the magnetic field is significantly sheared. Many of these active regions also host filaments, that is, structures consisting of plasma that is cooler and denser than its surroundings.

Magnetic flux ropes, i.e., twisted magnetic field lines that globally wrap around an axial magnetic field, are topological structures that can host and govern the dynamics of filaments (Kuperus & Raadu 1974; Démoulin & Priest 1989; Priest et al. 1989; van Ballegooijen & Martens 1989; Aulanier & Demoulin 1998; van Ballegooijen 2004; Mackay & van Ballegooijen 2006; Gunár & Mackay 2015). In addition, they can also explain the observed sigmoidal/highly sheared structures of erupting active regions (Canou & Amari 2010; Jing et al. 2010; Green et al. 2011; Savcheva et al. 2012; Gibb et al. 2014; Jiang et al. 2014). Structures compatible with magnetic flux ropes have also been found in solar cavities (Gibson et al. 2010; Rachmeler et al. 2013).

This evidence suggests that magnetic flux ropes play a fundamental role in solar eruptions, and explains why virtually all CME-initiation models have a phase in which a magnetic flux rope is present (see reviews by Forbes 2010; Chen 2011; Aulanier 2014; Filippov et al. 2015).

Based on the observation that many filament eruptions are associated with convergence motions toward the polarity-inversion line (PIL) of active regions, van Ballegooijen & Martens (1989) proposed flux cancellation at the PIL as a possible mechanism for the formation and eruption of magnetic flux ropes. This eruption scenario has been further investigated

in 2D by Forbes & Isenberg (1991) and Isenberg et al. (1993) by using an ideal magnetohydrodynamic (MHD) description of a magnetic flux rope embedded in the field generated by a sub-photospheric line dipole. In particular, these authors studied the evolution of the system in the equilibrium manifold when convergence flows toward the PIL were applied. In response to this photospheric driver, the magnetic flux rope follows a series of nearby equilibria that are located at larger and larger heights. This evolution continues until a critical point is reached. At this point, no nearby equilibrium is accessible and the system experiences a catastrophic *loss of equilibrium*: the magnetic flux rope suddenly jumps to a new equilibrium at a significantly larger height, and eventually experiences a full eruption if magnetic reconnection is allowed (Lin & Forbes 2000).

Another ideal-MHD mechanism for the initiation of CMEs is the *torus instability* (Bateman 1978; Kliem & Török 2006). In this model, a current ring of major radius R is embedded in an external magnetic field. Owing to the curvature of the current channel, the ring experiences a radial "hoop force," which is directed outward and decreases in magnitude if the ring expands. If the inwardly directed Lorentz force due to the external field decreases faster with R than the hoop force, the system becomes unstable.

Assuming an external field $B_{\mathrm{ex}} \propto R^{-n}$, the decay index n is defined as

$$n = -\frac{d\,\ln B_{\mathrm{ex}}}{d\,\ln R}. \tag{1}$$

Bateman (1978) and Kliem & Török (2006) showed that this instability occurs when $n \geqslant n_{\mathrm{crit}} = 1.5$. In other words, if the current ring has a major radius, R, such that the decay index of the external field, n, is significantly smaller than n_{crit}, the system is in a stable equilibrium where the inwardly directed magnetic tension of the external field balances the outwardly directed magnetic pressure of the current channel. However, if

$n \geqslant n_{\mathrm{crit}}$, then this equilibrium is unstable and any displacement of the current channel due to some perturbation will initiate an outward motion of the current ring.

By using a current-wire approach, Démoulin & Aulanier (2010) have shown that the torus instability is equivalent to a loss of equilibrium. In fact, the torus instability is the instability that occurs at the critical point of the equilibrium manifold of the loss-of-equilibrium model (Kliem et al. 2014).

The exact critical value of the decay index, n_{crit}, at which the loss of equilibrium occurs depends on the morphology of the current wire. If thin current distributions are considered, then $n_{\mathrm{crit}} = 1$ for an infinitely long wire, and $n_{\mathrm{crit}} = 1.5$ for a perfectly circular current ring. If relatively thick current distributions are considered, then the difference between n_{crit} for a straight wire and a circular ring is smaller. The current distributions found in MHD calculations are typically thick: the radius of the cross section is significant compared to the length of the current channel. For relatively thick current distributions the critical decay index lies in the range $n_{\mathrm{crit}} = 1.1$–1.3 or $n_{\mathrm{crit}} = 1.2$–1.5, depending on whether or not the current wire expands during the perturbation (Démoulin & Aulanier 2010). Independently of the exact topology of the external field, Kliem et al. (2014) have found that for a T&D (Titov & Démoulin 1999) flux rope the instability occurs when the critical decay index is $n_{\mathrm{crit}} \simeq 1.4$. Olmedo & Zhang (2010) analytically investigated the stability properties of a line-tied partial torus and found that the critical decay index for the onset of the instability is in the range of $n_{\mathrm{crit}} \approx 0.5$–$2$, depending on which fraction of the torus—from half to a full torus—is above the photosphere.

The aforementioned results are derived using wire models, that is, the equilibrium properties are determined by solving the momentum equation in terms of the current distribution. In recent years, many numerical experiments have been performed to validate the torus instability model using the full set of MHD equations. Török & Kliem (2005, 2007) performed numerical MHD simulations of a line-tied T&D flux rope embedded in different external magnetic field configurations and found that at the moment of the eruption the decay index at the apex of the flux rope axis is $n_{\mathrm{crit}} \simeq 1.5$. A similar value was found in a simulation where the magnetic flux rope is dynamically formed through magnetic reconnection at bald patches and at hyperbolic flux tubes (Aulanier et al. 2010). However, flux emergence simulations seem to suggest a higher value of the critical decay index. For example, Fan & Gibson (2007) and Fan (2010) have found that the critical decay index at the onset of the eruption lies in the range $n_{\mathrm{crit}} = 1.75$–1.9, while An & Magara (2013) found values for n_{crit} that are well above 2. Recently, MHD relaxations of nonlinear force free (NLFF) equilibria of solar active regions suggest values of the critical decay index in the range $n_{\mathrm{crit}} = 1.5$–1.75 (Kliem et al. 2013; Amari et al. 2014; Inoue et al. 2015).

It is clear that different studies give rise to significantly different critical values of the decay index for the onset of the instability. Therefore, it is natural to ask why so many different values exist.

Many of the basic concepts developed for the torus instability (such as the decay index) were developed in the current-wire framework. Applying these concepts directly to MHD calculations is difficult owing to the differences between the two approaches. First, there is the problem of identifying *where* to evaluate the decay index, n, to compare to the critical value n_{crit}. There is no ambiguity in the current-wire models—the decay index is always computed at the apex of the infinitesimal current wire. However, an equivalent structure does not generally exist in an MHD simulation, so it is unclear where to evaluate Equation (1). A natural choice is to follow the idealized case and compute n at the axis of the flux rope, but generally the axis is not well defined unless the rope is symmetric. Second, it is difficult to determine which n_{crit} should be used. In the current-wire formulation, different values of n_{crit} are derived for different prescriptions of the current profile in the wire. Generally, the current distribution of an MHD calculation will not match any of the idealized configurations. Finally, the current-wire approach often does not include the effect of line tying, which also affects n_{crit}. Given these problems, one might expect the two approaches to predict significantly different values for the onset of the instability.

However, and even more importantly, different MHD simulations result in different values of the critical decay index, raising further questions: What is the role of different line-tied photospheric drivers? Does the morphology of the magnetic flux rope also influence the critical value of the decay index in the MHD treatment? Does the current distribution within the flux ropes, which differs in different simulations, affect the critical value of the decay index? Can the different critical values of the decay index be due to the identification of the axis of the magnetic flux rope?

In order to address these questions, in the present paper we perform a parametric study aimed to determine the value of the critical decay index at the onset of the loss of equilibrium, when different classes of photospheric motions—which resemble the ones typically observed in active regions—are applied. Starting from an asymmetric, bipolar active region as in Aulanier et al. (2010), we apply four different classes of motions, namely, convergence toward the active region's PIL, asymmetric stretching, and peripheral and global dispersal of the active region. We describe how the corona responds to the different drivers and how these drivers affect the height and only marginally the critical value n_{crit} of the onset of the torus instability.

The plan of our paper is as follows. In the following section we introduce our numerical model, the initial condition, and the implementation of the boundary conditions. The topological and energy evolution of the system in response to these flows is presented in Section 3. Section 4 describes the analysis that we performed in order to determine the critical value of the decay index at the onset of the eruptions. Finally, in Section 5 we discuss our findings and conclude.

2. MODEL SETUP

The dynamics of the formation and evolution of magnetic flux ropes is modeled by using a new hybrid MPI/OpenMP parallel version of the Observationally driven High-order Magnetohydrodynamics code (OHM; Aulanier et al. 2005, 2010). The OHM-MPI code solves the following zero-β (pressureless), time-dependent MHD equations in Cartesian coordinates:

$$\frac{\partial \rho}{\partial t} = -\nabla \cdot (\rho \boldsymbol{u}) + \xi \Delta (\rho - \rho_0), \qquad (2)$$

$$\rho \frac{\partial \boldsymbol{u}}{\partial t} = -\rho (\boldsymbol{u} \cdot \nabla)\boldsymbol{u} + \boldsymbol{J} \times \boldsymbol{B} + \rho \nu' \mathcal{D} \boldsymbol{u}, \qquad (3)$$

$$\frac{\partial \boldsymbol{B}}{\partial t} = \nabla \times (\boldsymbol{u} \times \boldsymbol{B}) + \eta \Delta \boldsymbol{B}, \qquad (4)$$

$$\nabla \times \boldsymbol{B} = \mu \boldsymbol{J}, \qquad (5)$$

where ρ is the mass density (ρ_0 is its initial value at $t = 0$), $\boldsymbol{u}$ is the plasma velocity, $\boldsymbol{B}$ is the magnetic field, $\boldsymbol{J}$ is the electric current density, η is the magnetic resistivity, and μ is the magnetic permeability of the vacuum. $\xi \Delta (\rho - \rho_0)$ and $\nu' \mathcal{D}$ are artificial diffusion operators for the density and the velocity, whose presence is necessary to ensure the numerical stability of the code (see Aulanier et al. 2005, for details). Furthermore, in the continuity equation an extra "Newton's term" is added for $z \in [0, 0.7]$ in order to avoid sharp density variations close to the bottom boundary.

The calculation is parallelized using a combination of the OpenMP (Chandra et al. 2001) and the message passing interface (MPI) standards (Gropp et al. 1999). For OHM-MPI, OpenMP is used to distribute work among cores on individual nodes, while MPI is used to pass data between nodes. The computational volume is sliced horizontally (i.e., in x-y plane) to produce a vertical stack of subvolumes. Each node is assigned the task of computing the solution in a particular subvolume (which is itself divided among the cores on the particular node). At each time step, synchronization and data transfer between nodes are necessary to compute derivatives across subvolume boundaries. The parallelization achieves a significant speed-up for a moderate number of cores (~100); however, for large numbers of cores, the calculation is limited by the finite memory bandwidth in the shared memory environment and the communication times in the distributed memory environment.

The three-dimensional MHD equations are solved on a nonuniform mesh that covers the physical domain [−10, 10] × [−10, 10] × [0, 30] using 251 × 251 × 231 grid points with a grid resolution that varies in the range [6 × 10⁻³, 0.32] × [6 × 10⁻³, 0.32] × [6 × 10⁻³, 0.6], and with the smallest cell centered at $x = y = z = 0$. Similarly to Aulanier et al. (2010), the MHD equations are solved in their dimensionless form.

2.1. Initial Condition

As an initial condition for the magnetic field we consider the current-free (potential) field generated by two unbalanced monopoles placed at a distance $L = 2$ from each other and located at different depths below the photosphere ($z = 0$). The mathematical form of this field is (Aulanier et al. 2010)

$$B_x(t = 0) = \sum_{i=1}^{2} C_i (x - x_i) r_i^{-3},$$

$$B_y(t = 0) = \sum_{i=1}^{2} C_i (y - y_i) r_i^{-3},$$

$$B_z(t = 0) = \sum_{i=1}^{2} C_i (z - z_i) r_i^{-3},$$

$$r_i = \sqrt{(x - x_i)^2 + (y - y_i)^2 + (z - z_i)^2}, \qquad (6)$$

where ($x_1 = 1.025$; $y_1 = 0.3$; $z_1 = -0.9$; $C_1 = 15$) and ($x_2 = -0.775$; $y_2 = -0.3$; $z_2 = -1.3$; $C_2 = -14$). This initial condition results in an asymmetric active region with a positive flux excess of about 24%.

The initial density profile is defined as

$$\rho(t = 0) = B^2(t = 0), \qquad (7)$$

resulting in a uniform Alfvén speed ($c_A = 1$) everywhere in the computational domain. This ensures that if the boundary motions are sub-Alfvénic at the photosphere ($z = 0$), then they are sub-Alfvénic everywhere, therefore avoiding the generation of steep wavefronts at larger heights. The initial velocity field is $\boldsymbol{u} = 0$ in the entire computational domain.

2.2. Boundary Conditions

We impose zero-gradient, "open" boundary conditions for all the MHD variables at all the boundaries except for the boundary at $z = 0$, where we impose the so-called line-tied boundary conditions, therefore ensuring that the footpoints of each magnetic field line do not move unless the motions are explicitly prescribed (Aulanier et al. 2005).

In order to quasi-statically evolve the initial potential magnetic field into a current-carrying magnetic field, at the line-tied boundary we impose the following velocity profile:

$$\boldsymbol{u}(t) = \gamma(t) \boldsymbol{u}_0(t), \qquad (8)$$

$$\boldsymbol{u}_0(t) = u_0^{\max} \psi_0(t) \left[\nabla_\perp \psi(t) \right] \times \boldsymbol{e}_z,$$

$$\psi(t) = \exp\left[-\psi_1 \left(\frac{B_z(z = 0; t)}{B_z^{\min}(z = 0; t)} \right)^2 \right], \qquad (9)$$

where $\psi_1 = 3.5$, $u_0^{\max} = 0.05 c_A$, and $\psi_0(t)$ is computed at every time step to guarantee that the maximum value of $\boldsymbol{u}_0(t)$ is always equal to $u_0^{\max}$, therefore ensuring the sub-Alfvénic character of the driving motions. The function

$$\gamma(t) = \prod_{i=0}^{1} \left[\frac{(-1)^i}{2} \tanh\left(2 \frac{t - t_i}{\Delta t} \right) + \frac{1}{2} \right] \qquad (10)$$

is used to ensure that the flows are smoothly increased (decreased) from zero to their steady value (from their steady value to zero) within a time interval $2\Delta t$ centered at $t = t_0$ ($t = t_1$). In what follows, we will only give the time t_i as the time when the flows and/or diffusion are switched on (switched off), however implying that this is achieved over a time interval $[t_i - \Delta t, t_i + \Delta t]$.

We choose $t_0 = 10 t_A$, $t_1 = 100 t_A$, and $\Delta t = 3 t_A$, that is, the photospheric motions are applied until $t = 100 t_A$, when they decrease to half of their steady value, and become infinitesimal after $t = 103 t_A$.

By construction these flows are asymmetric vortices centered around the local maxima of $|B_z|$, with the fastest velocity being reached close to the PIL and rapidly decreasing when moving away from it and toward the center of the magnetic field polarities. As a consequence, these flows induce shear close to the PIL, without significantly perturbing the magnetic field anchored around the center of the magnetic polarities.

In order to study the effect of different photospheric flows on the formation and stability of magnetic flux ropes, starting from time $t = 105 t_A$ we impose four different classes of flows resulting in four different simulations runs: convergence of the magnetic flux closest to the PIL ("Run C": convergence), asymmetric stretching along one direction only ("Run S": stretching), and peripheral and global dispersal of the magnetic field polarities ("Run D1, D2": dispersal).

To define these boundary conditions, we use Equation (8) where $\gamma(t)$ is given by Equation (10), with $t_0 = 105t_A$, $\Delta t = 3t_A$, and t_1 the time when the eruption becomes unavoidable. The time t_1 is determined through a series of relaxations runs (see Section 4.1). Finally, $\boldsymbol{u}_0(t) \equiv [u_x(t), u_y(t)]$ is defined as follows:

1. "Run C":

$$u_x^C(t) = \begin{cases} u_0^{\max} \psi_0(t)\, \partial_x \psi(t), & \text{if } u_x(t) \cdot B_z(t) \leqslant 0 \\ 0, & \text{otherwise} \end{cases}$$
$$u_y^C(t) = 0 \qquad (11)$$

2. "Run S":

$$u_x^S(t) = u_0^{\max} \psi_0(t)\, \partial_x \psi(t)$$
$$u_y^S(t) = 0 \qquad (12)$$

3. "Run D1":

$$u_x^{D1}(t) = u_0^{\max} \psi_0(t)\, \partial_x \psi(t)$$
$$u_y^{D1}(t) = u_0^{\max} \psi_0(t)\, \partial_y \psi(t) \qquad (13)$$

with $\psi(t)$, $\psi_0(t)$, ψ_1, $u_0^{\max}$ the same as in Equations (9) and

4. "Run D2":

$$u_x^{D2}(t) = u_0^{\max} \psi_0(t)\, \partial_x \psi(t)$$
$$u_y^{D2}(t) = u_0^{\max} \psi_0(t)\, \partial_y \psi(t) \qquad (14)$$

that is, exactly the same as "Run D1," but with $\psi_1 = -0.5$.

The different flow profiles, $\boldsymbol{u}_0(t)$, at the beginning of the convergence phase are shown in the left panels of Figure 1. The effect of these motions on the normal component of the magnetic field at $z = 0$ and at the end of the driving phase is shown in the right panels of Figure 1.

A comparison between the last two rows of Figure 1 illustrates the effect of the parameter ψ_1 in the function $\psi(t)$: it controls the size of the region (centered around the maximum of the polarity) that is unaffected by the flows. Finally, all the applied flows have a component that induces flux convergence toward the PIL. This is a common features of several CME's initiation scenarios, and it is very often observed to precede the onset of eruptive flares.

2.3. Diffusive Coefficients

The MHD equations solved by the OHM-MPI code include an artificial density diffusion coefficient ξ, a pseudo-viscosity ν', and a coronal resistivity η. These coefficients are required to ensure the numerical stability of the code. In addition, at the lower boundary a photospheric diffusion term η_p is also present.

Each of the four simulation runs described in this paper can be divided into three different phases: (1) the twisting phase driven by the boundary motions defined by Equation (8) and applied from $t = 0$ to $t = 100t_A$ (the same for all the simulations); (2) the convergence phase driven by the motions defined in Equations (11)–(14) from $t = 105t_A$ to $t = t_1$, i.e., the time when the eruption becomes unavoidable; and (3) the eruption phase, where we impose $u_x(z = 0, t) = u_y$
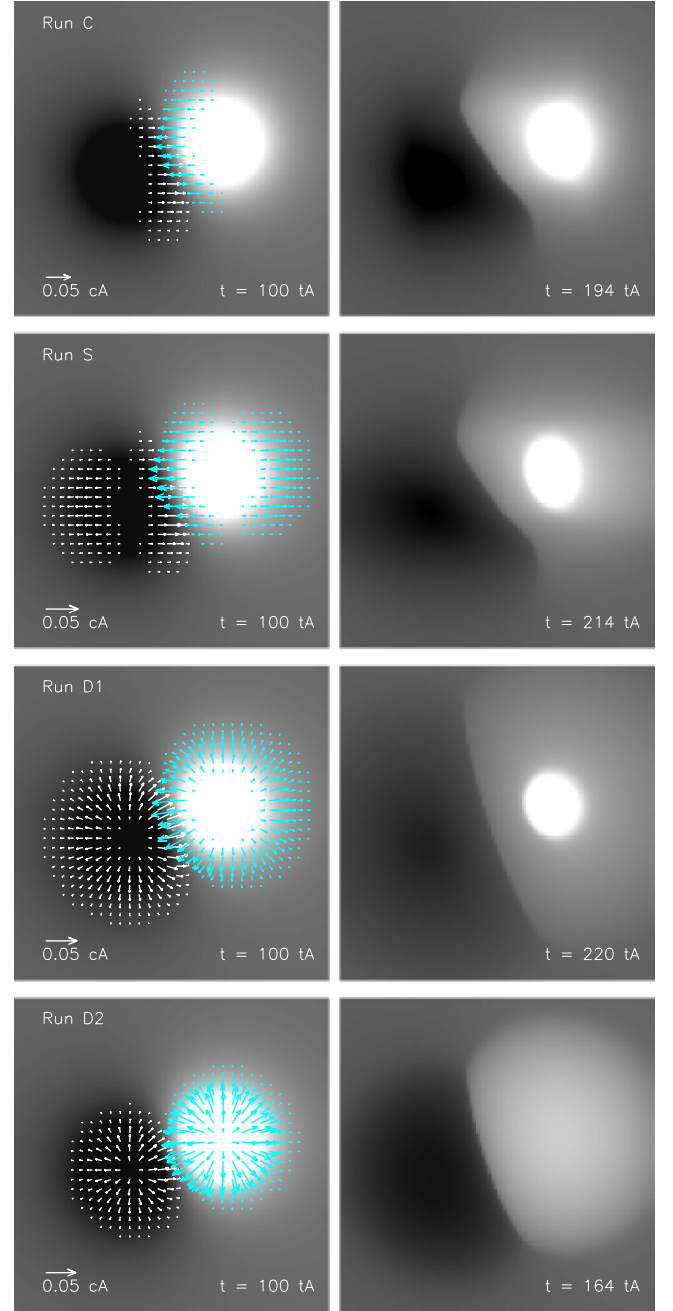

Figure 1. Maps of $B_z(z = 0)$ at the beginning (left) and end (right) of the convergence phase for "Run C," "Run S," "Run D1," and "Run D2" (first, second, third, and fourth row, respectively). White (black) color indicates positive (negative) magnetic field. Cyan/white arrows outline the initial velocity profile. The field of view is $x, y \in [-3.3, 3.3]$.

$(z = 0, t) = 0$, which begins from $t = t_1$ until the end of the simulations.

During the twisting and the convergence phases, the coronal diffusivity is fixed to $\eta_{cor} = 4.8 \times 10^{-4}$, the diffusion coefficient is $\xi = 1.5\eta$, and the pseudo-viscosity is $\nu' = 25$. At the smallest grid size these coefficients result in the following diffusive speeds: $u_\eta = 0.08$, $u_\xi = 1.5u_\eta$, and $u_{\nu'} = 0.15$. During the eruption phase, fast flows and sharp currents develop. Therefore, we fix $\eta_{cor_1} = 2.1 \times 10^{-3}$, $\nu'_1 = 41.7$, and $\xi_1 = \eta_{cor_1}$. This is required to ensure the numerical stability of the code.
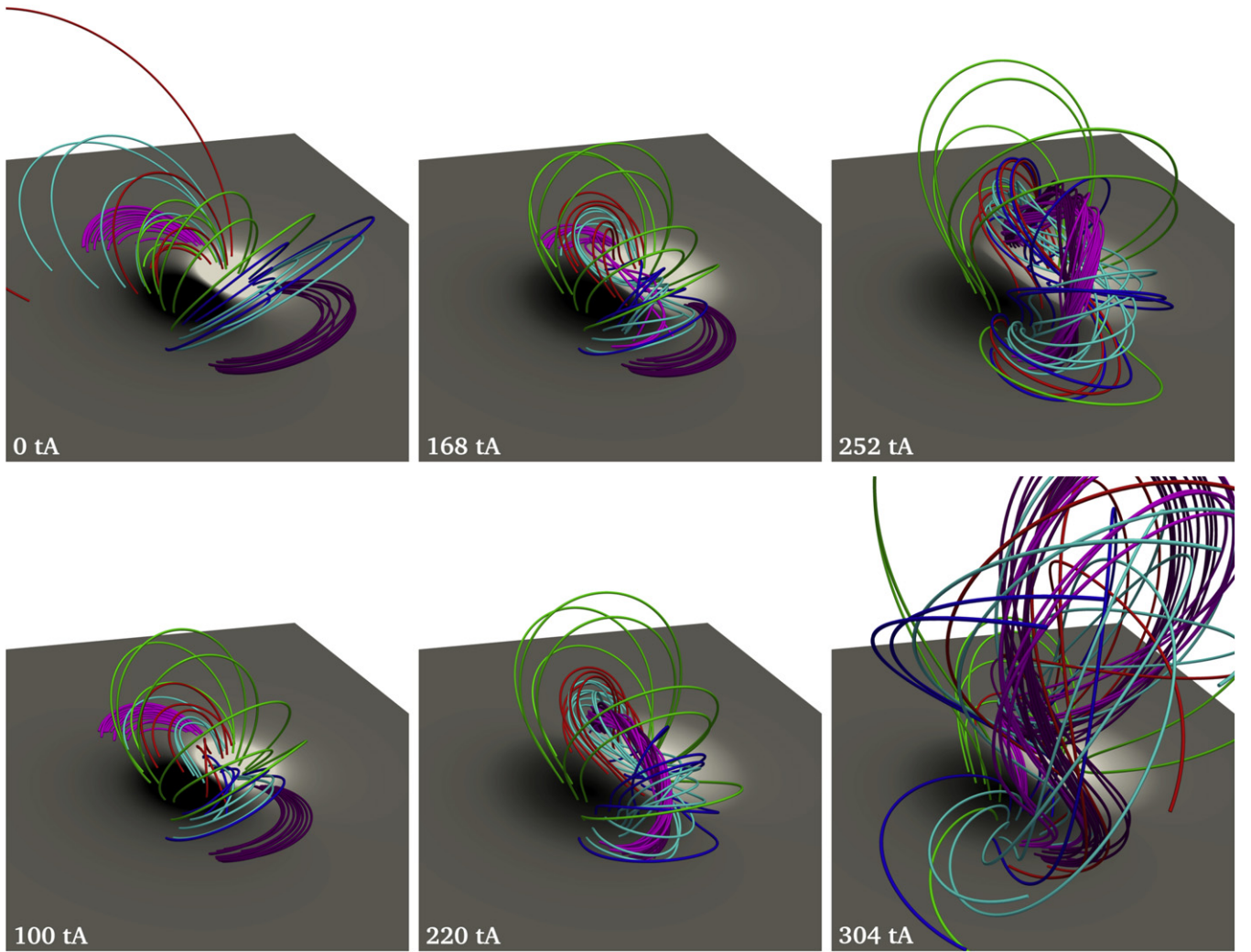
4

Figure 2. Evolution of the magnetic field for "Run D1" during the quasi-static shearing (left) and convergence (middle) phase and the eruptive phase (right panels). White (black) color indicates positive (negative) $B_z(z = 0)$.

At the line-tied boundary, the photospheric resistivity η_p is set to zero during the twisting phase. This allows the buildup of magnetic shear and current in the system without modifying the photospheric distribution of B_z and without forming a bald patch as in Aulanier et al. (2010). During the convergence phase, magnetic flux is advected toward the PIL with a rate that varies with time in a nonlinear way, but that is always smaller than $2u_0^{\max}$. Therefore, in order to avoid flux pileup at the PIL during the phase $t \in [100t_A, t_1]$, we impose a photospheric resistivity $\eta_p = \eta_{\text{cor}}$. We choose this value because it seems to be the best compromise between magnetic field diffusion and flux advection for a significant portion of the PIL. Finally, during the eruption phase ($t \geqslant t_1$) the photospheric diffusion is again set to zero. This eventually results in the onset of a numerical instability close to the boundary at $z = 0$ that originates from narrow photospheric current layers. This problem is resolved by artificially smoothing the Lorentz force within the first 22 grid points, i.e., for $z \in [0, 0.165]$. This is achieved by multiplying the Lorentz force in the momentum equation by a factor

$$\sigma_f = \frac{1 + \tanh[33(z - 0.08)]}{2}, \quad \forall\, z \in [0, 0.165]. \quad (15)$$

We choose this solution instead of an increased photospheric diffusion, because the latter would induce reconnection at the line-tied boundary and, more importantly, will essentially modify the reference potential field energy during the study of the instability.

3. DYNAMICS AND ENERGETICS

In this section the evolution of the system from the initial current-free configuration to the formation of the flux rope and its eruption is discussed. Although the timing and the onset of the eruption differ between the simulations, the overall topological evolution of the system is the same for the different runs. Therefore, we limit ourselves to the description of only one of the four simulations, namely, "Run D1," that is, a partial dispersal of the active region field.

3.1. Dynamical Evolution

The top left panel of Figure 2 shows selected magnetic field lines highlighting the initial potential magnetic field configuration of the system. In order to build up currents in the system at the line-tied boundary, we apply the velocity field defined in

Equation (8). As already mentioned, the applied motions are never larger then a few percent of the Alfvén speed, and, as a consequence, the coronal field evolves quasi-statically in response to the photospheric driver.

The configuration of the system after $100t_A$, i.e., at the end of the twisting phase, is shown in the bottom left panel of Figure 2. As is evident, the field lines close to the PIL (blue/red/cyan field lines) are the most sheared ones, while the overlying field (green field lines) only experiences a minor twist. During this phase, no magnetic flux rope is observed. Nevertheless, owing to the injected shear, the magnetic pressure starts to increase, especially in the proximity of the PIL, and the system slightly bulges up. In the simulation of Aulanier et al. (2010) this initial bulging up of the field lines close to the PIL, combined with the presence of a finite photospheric diffusion, resulted in a topological change of the system from sheared-arcade to a three-dimensional bald-patch configuration containing a bald-patch separatrix. Because we explicitly impose $\eta_p = 0$, no flux cancellation occurs close to the PIL and no change in the topology is observed during the twisting phase in our simulations, and hence no magnetic flux rope is formed yet.

The aim of this first driving phase is to obtain a quasi force-free field with a sheared-arcade topology. This constitutes the initial condition for our study of different classes of photospheric motions. These motions induce a deformation and evolution of the active region similar to what is often observed on the Sun.

Starting from this sheared-arcade configuration, we apply the four different boundary motions described in Equations (11)–(14). Figure 2 (middle panels) shows the response of the system to these drivers (for "Run D1").

As a consequence of the applied convergence motions, photospheric flux is advected toward the PIL, and since during this phase we impose a finite photospheric diffusion, similarly to Aulanier et al. (2010), we observe the transition from sheared-arcade to a bald-patch topology. Magnetic reconnection occurs at the bald patch, and a mildly twisted flux rope is formed.

The top middle panel of Figure 2 shows the configuration of the system during the buildup phase of the flux rope. The forming magnetic flux rope is highlighted by selected pink/purple/cyan field lines. Pink (purple) field lines are traced starting from the top (bottom) part of the positive (negative) polarity. Cyan field lines are traced starting from locations that are in between the pink/purple and the red/blue field lines. The red/blue field lines are traced starting at either side of the bald patch, actually highlighting the bald-patch separatrix below the magnetic flux rope. The figure also shows that the flux rope field lines are about twice as long as the field lines that extend at either side of the bald-patch separatrix.

While the convergence motions continue, more and more flux is advected toward and canceled at the PIL, and the bald-patch separatrix evolves. In particular, the photospheric footprints of the bald-patch separatrix continue to expand. The bottom middle panel of Figure 2 shows a snapshot of the system toward the end of this process and just before the onset of the instability (see Section 4). The purple and pink field lines show the main body of the flux rope. The cyan field lines show the outer layer of the flux rope, that is, the set of field lines belonging to the flux rope that come closest to the bald patch. Owing to the curvature of the flux rope axis, only those field

lines in the outer layer contain magnetic dips, while those close to the axis do not. This may be contrasted with an ideal cylindrical flux rope, where dips are present at all distances from the axis. The figure also shows how the flux rope is embedded between two set of sheared field lines (red/blue) and much less sheared (i.e., quasi-potential) overlying magnetic field (green field lines).

The formation phase of the magnetic flux rope is morphologically similar to—but topologically different from—what was observed in the simulation of Aulanier et al. (2010). In the latter, the bald-patch separatrix disappeared quite soon during the formation phase of the magnetic flux rope and was replaced by a quasi-separatrix layer. The reconnection that transferred flux from the overlying field to the magnetic flux rope occurred at the hyperbolic flux tube. However, in our simulations, the bald-patch separatrix is always present and the magnetic reconnection occurs at the bald patch only.

The top right panel of Figure 2 shows the early stages of the flux rope eruption. During this phase, photospheric diffusion is reset to zero and no boundary flows are applied. Therefore, the system only evolves in response to the imbalance between the magnetic pressure associated with the current-carrying magnetic flux rope and the magnetic tension of the overlying field. Furthermore, during the early stages of the eruption, the flux rope expands outward without any significant kink. When the flux rope enters the dynamical regime, sheared post-flare loops (not displayed in the figure) are formed below the current sheet, as already discussed in Aulanier et al. 2012. During this phase, the bald patch is still present, and bald-patch field lines are now low-lying field lines with the second footpoint anchored close to the central part of the PIL.

The continuous presence of bald patches in our simulations (in contrast with Aulanier et al. 2010) is probably due to the convergence motions. As a consequence of these motions, magnetic field is continuously advected toward the PIL at a rate that is comparable to the diffusion rate, and this maintains the bald-patch topology.

The final snapshot of the simulation is shown in the bottom right panel of Figure 2, just before the fast flows generated during the eruptive phase induce a numerical instability and halt the simulation. The flux rope undergoes a full eruption and, during the propagation, is deflected toward the lower left part of the domain. This deflection is probably a consequence of the asymmetry of the system. The positive polarity is more intense than the negative one, which results in a magnetic pressure gradient that is directed toward the lower left part of the domain. This kind of flux rope deflection has also been found in a simulation of a more complex, asymmetric active region (Zuccarello et al. 2012).

3.2. Energy Evolution

The evolution of the potential, free, and total magnetic energies, as well as of the kinetic energy for "Run D1," is shown in Figure 3. The same plots for the other simulation runs are presented in the appendix.

To compute the potential energy of the system for each snapshot, we perform a potential field extrapolation of the photospheric magnetic field $B_z(z = 0)$ using the method of Alissandrakis (1981). First, we extract the bottom boundary of the simulation and remap the nonuniform grid of OHM-MPI onto a uniform grid of [301 × 301] points, resulting in a uniform grid spacing of about 10 times the smallest OHM-MPI
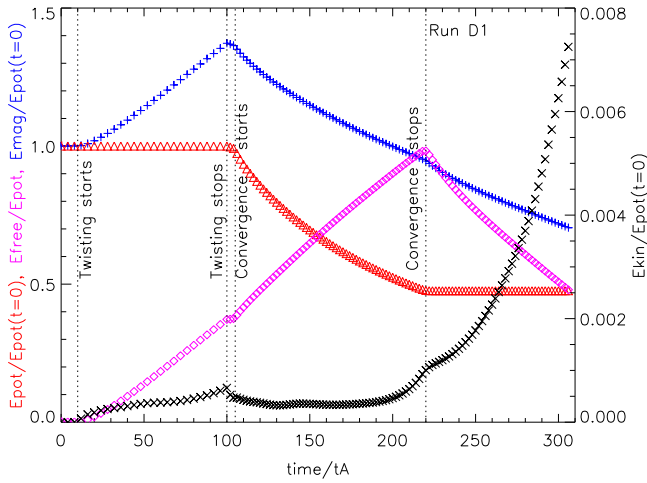
Figure 3. Temporal evolution of the free magnetic energy in the system (purple "◇") and of the kinetic (black "×"), potential (red "△"), and total (blue "+") magnetic energy of the system normalized to the energy of the initial (potential) magnetic field for "Run D1." The magnetic energy of the initial potential field is $E_{\mathrm{pot}}(t=0) = 174.4$.

grid cell. Second, in order to minimize the aliasing effects due to the intrinsically assumed periodic boundary of the fast Fourier transform method, the remapped OHM-MPI boundary is inserted at the center of an 8 times larger grid that is padded with zeros. With this method we achieve an accuracy in the magnetic energy computation, i.e., the difference between the energy of the reconstructed field and the energy of the field generated by the analytic charges of about 0.1%.

As a result of the nature of the twisting flows—which do not modify B_z at the boundary from $t = 10t_A$ to $t = 100t_A$—the potential energy of the system ("△") remains unchanged and the increase in the total magnetic energy ("+") is directly related to the increase of the free magnetic energy ("◇"). However, during the convergence phase, i.e., from $t = 105t_A$ to $t = 220t_A$, the distribution of B_z at the boundary is modified by the flows and the potential energy of the system changes, eventually reaching about half of its initial value. During this phase, the total magnetic energy also decreases; however, the free magnetic energy continues to increase. At the end of the convergence phase, the system has a free magnetic energy that is of the same order of the potential energy; therefore, about half of the total magnetic energy stored into the system is available for the eruption.

During the twisting and convergence phases, the kinetic energy always remains very low, eventually confirming that the system evolves quasi-statically. At about $t = 210t_A$ the kinetic energy starts to rise exponentially, but at $t = 220t_A$ the pseudo-viscosity is increased (Section 2.3) and the initial rise of the kinetic energy is smoothed out for about 5–10t_A. After that, the exponential increase of the kinetic energy continues until the end of the simulation. As a final remark, we note that the kinetic energy constitutes only a very moderate fraction ($\sim$4%) of the free magnetic energy released during the eruption.

4. ERUPTION ONSET AND TRIGGER

The dynamical evolution of the system and the previous results of Aulanier et al. (2010) suggest that the torus instability

is the trigger of the flux rope eruptions presented in this paper. Moreover, as discussed by Démoulin & Aulanier (2010), the exact value of the critical decay index at the onset of the eruption may be different depending on the exact morphology of the flux rope.

To clarify these points, in this section we present the analysis that we performed in order to determine (1) the value of the critical decay index at the onset of the eruption and (2) whether the torus instability is the trigger of our eruptions. In particular, we first determine the moment of the eruption (i.e., t_1) by performing relaxation runs, and then, around the moment of the eruption, we identify the axis of the flux rope and compute the decay index at different heights. Finally, we determine the value of the decay index at the height of the flux rope axis for both eruptive and noneruptive runs.

In the following subsections the different stages of our analysis are described in detail.

4.1. Relaxation Runs

In order to determine the time of the onset of the eruptions, at different times t^* during the convergence phase we impose $\boldsymbol{u}_0(t \geqslant t^*) = 0$, $\eta_p = 0$ and let the system evolve. The photospheric flows are always slowed down by using the function $\gamma(t)$ defined in Equation (10). The first time t^* for which the eruption becomes unavoidable defines the time t_1 discussed in Section 2.2 and Equation (10).

For "Run C" we find that for $t^* = 188t_A$ no eruption occurs, while for $t^* = 192t_A$ the flux rope erupts, but it gets deflected. In fact, at the initial phase of the instability onset the magnetic pressure of the magnetic flux rope is just enough to overtake the magnetic tension of the overlying field, and the flux rope starts to ascend. Owing to the asymmetry of the configuration, the magnetic field of the positive polarity is larger than the one of the negative polarity, and a magnetic pressure gradient exists. During the early stages of the eruption, this pressure gradient influences the dynamic of the flux rope, eventually deflecting it toward the lower left boundary. If the photospheric motions for "Run C" are stopped at $t^* = 196t_A$, the flux rope experiences a "full eruption," like the one discussed in Section 3. During this extra time, extra current-carrying magnetic flux (and hence magnetic pressure) is injected into the flux rope, eventually mitigating the effect of the asymmetric pressure gradient due to the external field.

It should be noted that the deflection of the magnetic flux rope is observed also in the "fully eruptive" runs (Section 3) but develops at a later stage. For the fully eruptive runs the pressure gradient associated with the flux imbalance influences only the propagation of the magnetic flux rope rather than its initial dynamics.

For "Run S" we observe a similar behavior. If we stop the photospheric driver at $t^* = 206t_A$, the system finds a new equilibrium, while if the photospheric driver is switched off at $t^* = 210t_A$, an eruption occurs but undergoes a very strong deflection toward the boundary. If $t^* = 214t_A$, a full eruption occurs.

For "Run D1" ("Run D2," respectively) the evolution is slightly different. If the photospheric driver is interrupted at $t^* = 216t_A$ ($t^* = 160t_A$, respectively) no eruption occurs, but if the driving is stopped four Alfvén times later, i.e., at $t^* = 220t_A$ ($t^* = 164t_A$, respectively), the system undergoes a full eruption without displaying the deflection that is observed for "Run C" and "Run S." One of the differences between "Run
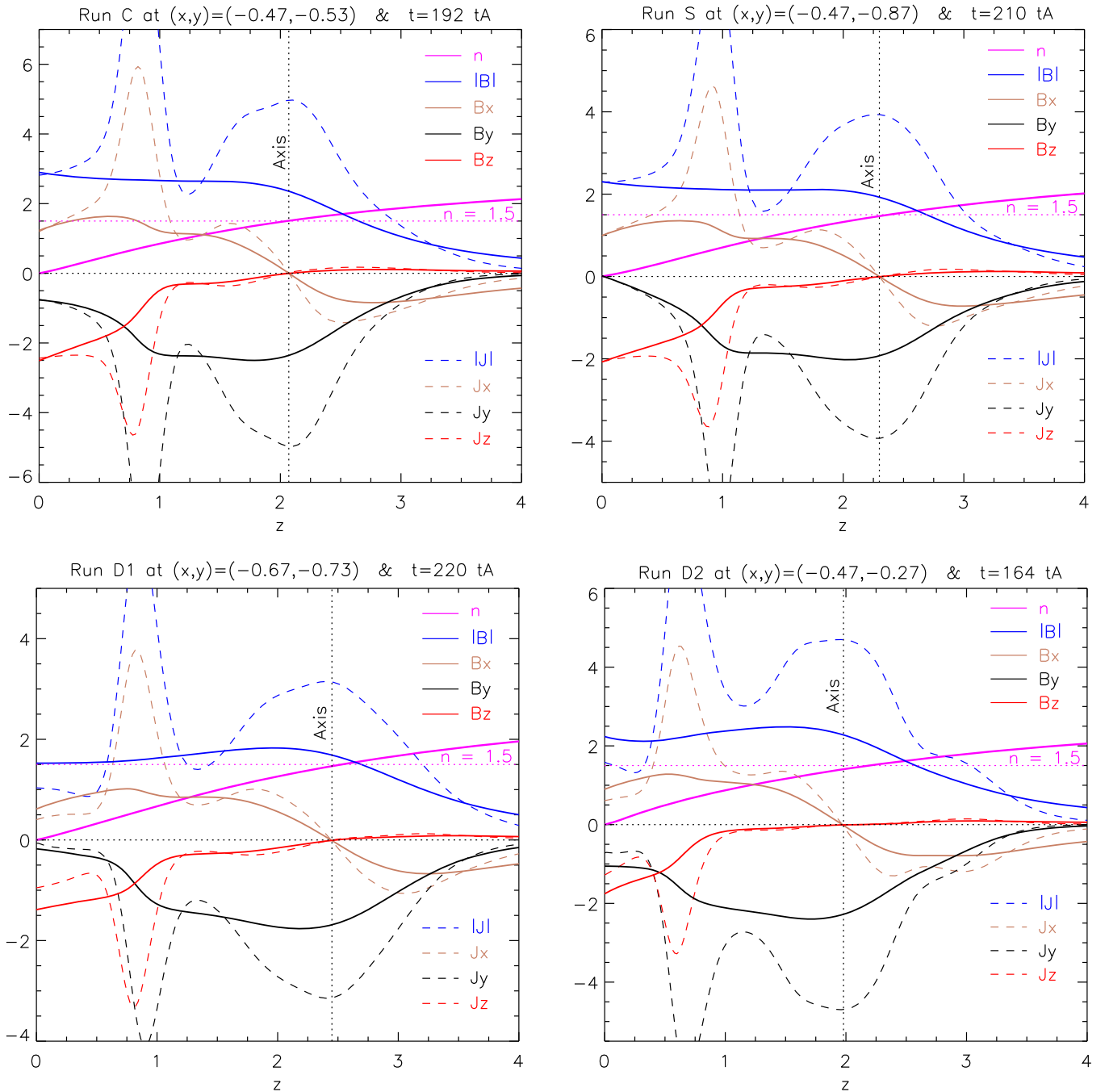
Figure 4. Vertical dependence of the norm, x, y, and z components (blue, brown, black, and red lines) of the magnetic field (solid lines) and current density (dashed lines), as well as of the decay index (solid purple line) at a given (x, y) position and time t (indicated in each panel) for "Run C," "Run S," "Run D1," and "Run D2" (from top left to bottom right, respectively). The vertical dotted line indicates the height where both B_x and B_z change sign.

C, S" and "Run D1, D2" is that in the latter the prescribed motions are perpendicular to the PIL, while the former ones are parallel to the x-axis, inducing a photospheric flux distribution that eventually increases the original asymmetry (and magnetic pressure imbalance) of the overlying magnetic field.

4.2. Flux Rope Axis

Magnetic flux ropes are generally defined as an ensemble of twisted magnetic field lines that wrap around a common central axis. However, when the twist is $\lesssim 2\pi$, the wrapping is not full and the identification of the axis of the magnetic

flux rope is difficult. As a consequence, a unique criterion fo`r the identification of the axis of a magnetic flux rope does not exist, and different cases should be analyzed individually.

For curved flux ropes that are in equilibrium with an external magnetic field, the apex of the flux rope's axis must lie along the local PIL. Therefore, at the location of the apex, B_z must change sign. Moreover, in our simulations the flux rope (at least the highest part of it) is almost parallel to the y-axis; therefore, at the height of the axis, B_x must change sign - with the height z.

To determine the axis of the magnetic flux rope, we then proceed as follows. For the simulation output at time $t = t_1$ ($192t_A$, $210t_A$, $220t_A$, $164t_A$ for Runs C, S, D1, D2, respectively), we look at the three components of the magnetic field along vertical lines passing through different $[x; y]$ positions along the PIL. Among the different positions, we look for the one $[\bar{x}; \bar{y}]$ where the change in sign of B_x and B_z occurs at the same height $z = \bar{z}$. The axis of the magnetic flux rope (see yellow tube in Figure 6 below) is then assumed to be the magnetic field line that passes through the position $[\bar{x}; \bar{y}; \bar{z}]$ at time $t = t_1$.

Figure 4 shows the norm and the three components of the magnetic field (solid lines) and of the current density (dashed lines) along the vertical z-axis that passes through $[\bar{x}; \bar{y}]$.

The vertical dotted line indicates the height $\bar{z}$ where both B_x and B_z change sign, that is, the height of the apex of the magnetic flux rope's axis. As is evident, the apex of the magnetic flux rope does not have the same position in all the simulations. In particular, for "Run C" and "Run D2" the eruption begins at a lower height than in "Run S" and "Run D1."

Interestingly, we find a posteriori in Figure 4 that the current density has a local maximum along the axis of the magnetic flux rope and is almost aligned with it ($J \simeq |J_y|$). This behavior is quite similar to what is expected for a flux rope generated by a relatively thick current wire or an NLFF cylindrical constant-twist (Gold–Hoyle) flux rope. Closer to the photosphere the maximum of the norm of the current density highlights the narrow current layer associated with the bald-patch separatrix. This is the region where magnetic reconnection occurs, eventually transferring flux from the overlying field into the flux rope field.

4.3. Decay Index

The magnetic field that is relevant to compute the decay index is the so-called external field, which is not associated with the coronal currents. In the symmetric configurations where the torus instability has been originally formulated the "external field" is the one generated by the sub-photospheric charges. At the axis of the flux rope, it has only a toroidal component.

We use the potential field associated with the photospheric distribution of $B_z(x, y, z = 0)$ at time $t = t_1$ (see Section 3.2) as the external field to be used for the computation of the decay index. Furthermore, to account for the intrinsic asymmetry of our model, only the horizontal component of the reconstructed potential field is used.

Two-dimensional maps of the decay index for different heights and for the four different simulations are shown in Figure 5. Only the contours where $n = 1$, 1.25, and 1.5 are shown (for "Run D2" an extra contour at $n = 1.4$ is also included). The yellow (orange) line indicates the PIL of the potential field (in the simulation) at any given height. Finally, the white square indicates the $[\bar{x}, \bar{y}]$ position of the apex of the magnetic flux ropes as determined in Section 4.2.

Figure 5 (first row) shows maps of decay index for "Run C." The contour $n = 1.5$ touches the local PIL of the simulation (i.e., the PIL of the flux rope) at a height $z \simeq 2$. This is remarkably close to the height of the axis of the magnetic flux rope at $t = 192t_A$ (Figure 4, top left), when the deflected eruption began.

For "Run S" at the onset of the eruption, the axis of the magnetic flux rope has a height $z \simeq 2.3$. Figure 5 (second row) shows that the critical value $n = 1.5$ of the decay index at the location of the apex of the magnetic flux rope's axis is reached between $z = 2.2$ and $z = 2.4$. This is in very good agreement with the original $n_{\rm crit} = 1.5$ of the torus instability scenario. A similar conclusion can be drawn also for "Run D1," where the actual value of the decay index at the position of the apex is $n_{\rm crit} \simeq 1.45$ (Figure 4, bottom left, and Figure 5, third row).

From the bottom right panel of Figure 4 we can deduce that for "Run D2" the eruption begins when the flux rope axis has a height $z \simeq 1.95$. As is evident, the decay index at the apex of the magnetic flux rope's axis (purple curve) has not yet reached the value $n = 1.5$. This is more evident in Figure 5 (fourth row): at $z = 2$ the contour $n = 1.4$ has already touched the PIL, while the contour $n = 1.5$ touches the PIL only at $z = 2.2$. This seems to suggest that for "Run D2" the critical decay index for the onset of the eruption is about 7% smaller than for the other three cases.

4.4. Unique Critical Decay Index?

The results of the performed analysis are synthesized in Figure 6. In this figure for the simulation runs that exhibited an initial deflection, i.e., "Run C" and "Run S," three different snapshots around the moment of the onset of the eruption are presented. For "Run D1" and "Run D2" no deflected eruption is observed, and therefore only two snapshots around the onset time are shown.

For each snapshot of the same row (i.e., same boundary flow profile), the magnetic field lines are traced starting from the same footpoints and are color-coded with the current density. The thicker yellow field line represents the axis of the magnetic flux rope as identified in Section 4.2. The purple semitransparent plane represents the critical height (different for each simulation) where the contour $n = 1.5$ of the decay index touches the PIL of the simulation. This height is $z = 2$, 2.3, 2.5, and 2.2 for Runs C, S, D1, and D2, respectively (see Section 4.3 and Figure 5).

For each of the simulations the configuration displayed in the left panels is stable, i.e., no eruption occurs if the photospheric driver is stopped (see Section 4.1). It is evident from Figure 6 (left panels) that at this time the axis of the magnetic flux rope has not yet reached the height where $n = 1.5$ and no eruption occurs.

For the two deflected eruptions, i.e., "Run C" and "Run S," the middle panels of Figure 6 (top two rows) report the configuration of the system when the deflected eruptions occur. As is evident, the axis of the flux rope has reached the height where $n = 1.5$, and even if we stop the driver now, the eruption occurs anyway. The system has entered an unstable regime and evolves, driven by the imbalance between the magnetic pressure of the flux rope and the magnetic tension of the overlying field. It is very interesting that for these two simulations the critical value for the onset of the torus instability is remarkably close to the theoretical value for a thin circular current ring (Démoulin & Aulanier 2010). Finally, if we switch off the flows four Alvén times later (Figure 6, two top right panels), the axis of the magnetic flux rope is well above the theoretical critical height and the eruption develops without any deflection (apart from the interaction with the boundary during the propagation). As already mentioned in Section 4.1, this is probably due to the extra magnetic
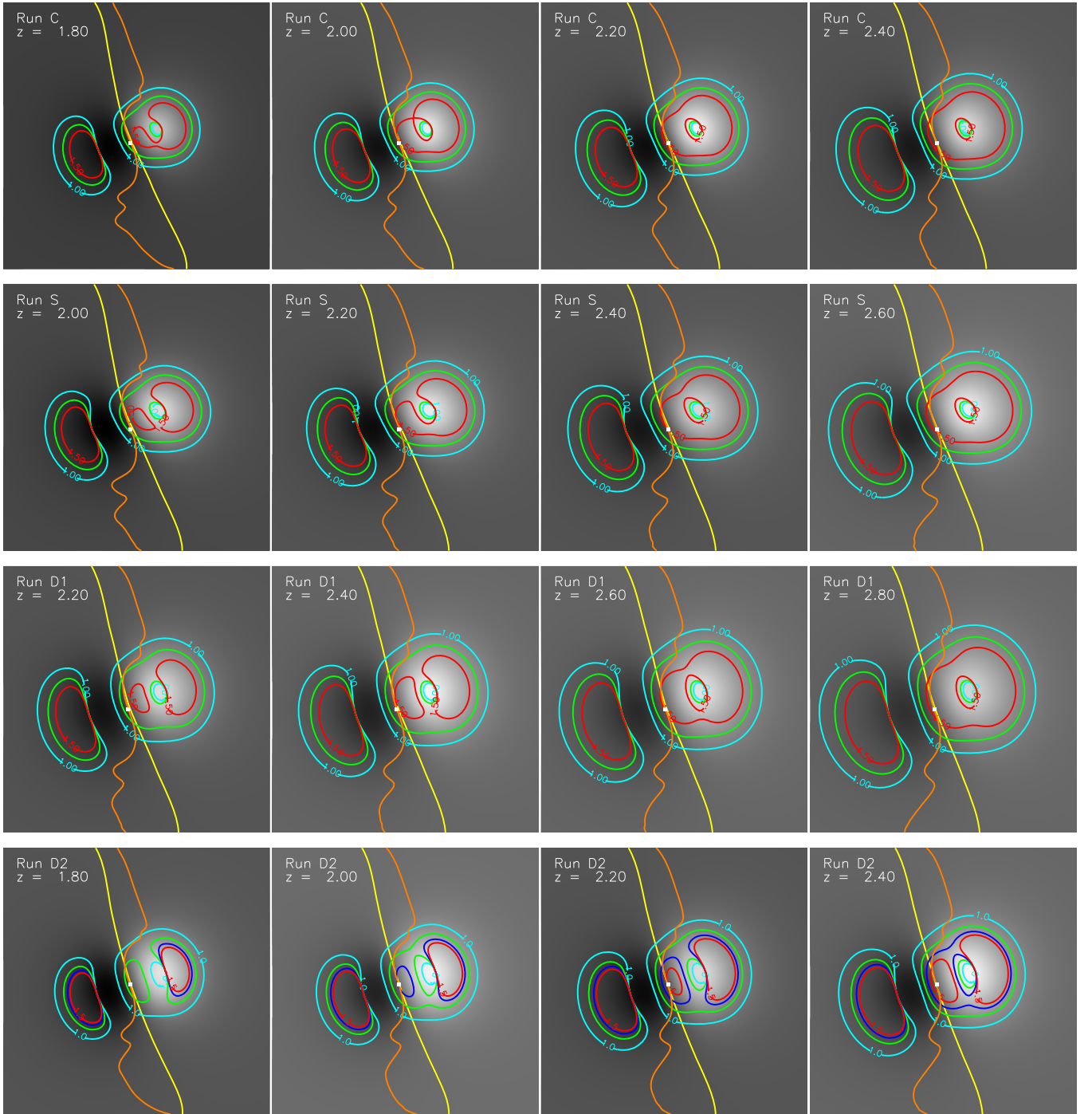
Figure 5. Two-dimensional maps of contours of the decay index—$n = 1$ (cyan), $n = 1.25$ (green), $n = 1.5$ (red)—overplotted to the normal component of the magnetic field at different heights for "Run C," "Run S," "Run D1," and "Run D2" (first, second, third, and fourth row, respectively). For "Run D2" the contour of the decay index at $n = 1.4$ (dark blue) is also shown. The orange (yellow) line indicates the PIL of the simulated (extrapolated) magnetic field. The white square indicates the $(x; y)$ position of the apex of the flux rope's axes. The extrapolations have been performed at times $194t_A$, $214t_A$, $220t_A$, and $164t_A$ for Runs C, S, D1, and D2, respectively.

pressure built into the flux rope during the extra convergence time.

Figure 6 (two bottom right panels) show the eruptive configuration for "Run D1" and "Run D2." As is evident, for both simulations the axis of the magnetic flux rope has not yet reached the height where $n = 1.5$ (semitransparent purple plane), but the eruption occurs anyway. As can be deduced

from the previous section, the value of the decay index is $n_{crit} \simeq 1.4$–1.45, that is, still very close to $n = 1.5$.

4.5. The Effect of the Diffusion Coefficients

During the eruption, strong flows originate at the current sheet that develops below the erupting flux rope, eventually
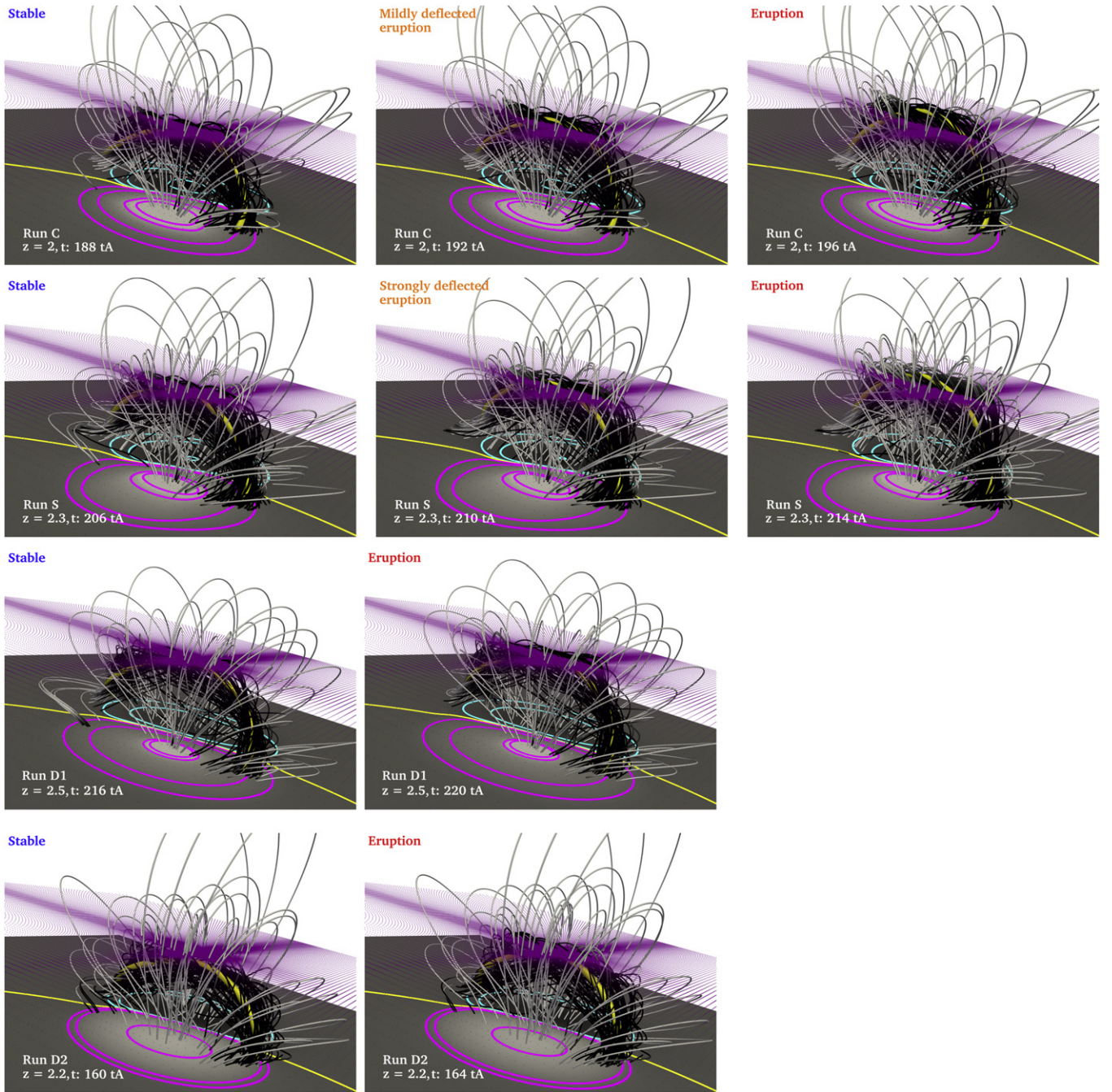
Figure 6. Snapshots around the time of the instability onset for "Run C," "Run S," "Run D1," and "Run D2" (first, second, third, and fourth row, respectively). The purple semitransparent plane indicates the height (z)—as deduced from Figure 5—where the contour of the decay index, $n = 1.5$, touches the part of the PIL occupied by the flux rope. The field lines are color-coded with the magnitude of the current density using the same difference between the low and upper limits of the color scale.

resulting in a numerical instability and halting the simulation. As discussed in Section 2.3, this can be resolved by increasing the diffusion coefficients. In order to minimize the variation between the different runs, the relaxation runs are performed with the same conditions as the eruptive ones. In other words, at time $t = t_1$ not only are the flows switched off, but the coronal diffusive coefficients are also modified according to what is discussed in Section 2.3. This results in an over-estimation of the critical value of the decay index.

The system approaches the critical point for the onset of the instability in an environment that is characteristic by "low"

diffusion coefficients. Under this condition, current is built up into the magnetic flux rope through magnetic reconnection at the bald patch and slowly rises. At a certain moment, it reaches the height where $n = n_{crit}$ and starts to accelerate under the effect of the torus instability. However, at the same time, we increase the coronal diffusivity by a factor of 4.37, eventually suddenly dissipating part of the magnetic flux rope's current and bringing the flux rope back to the equilibrium curve. Therefore, in order for the eruption to occur, extra current, behind the amount required under "low" diffusion conditions, must be injected into the flux rope to account for the increased
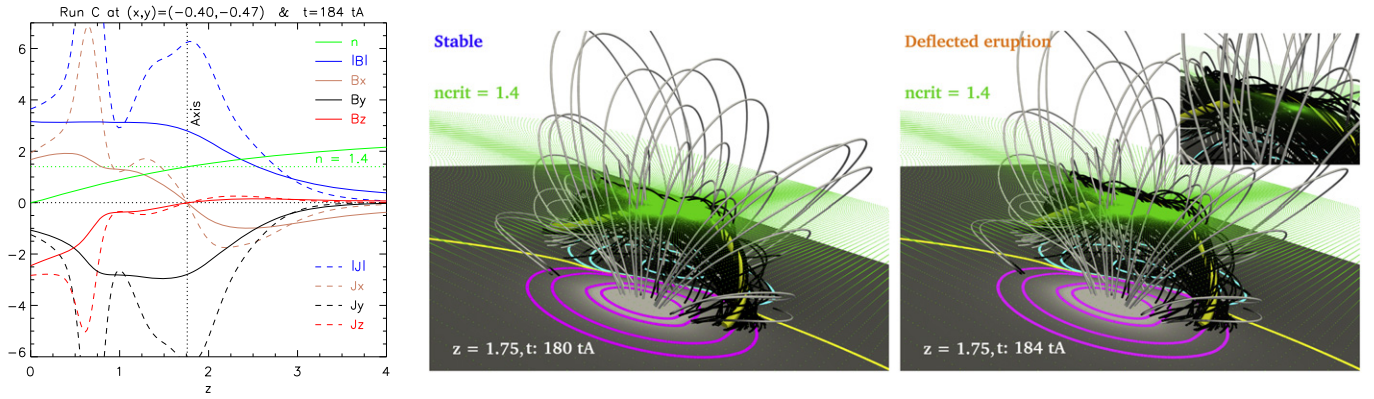
Figure 7. Left panel: same as Figure 4 but for "Run C" under "low" coronal diffusion conditions. Middle and right panels: two snapshots around the time of the instability onset for "Run C" under "low" coronal diffusion conditions. The green semitransparent plane indicates the height (z) where the critical decay index at the apex of the magnetic flux rope is $n_{crit} = 1.4$. The field lines are color-coded with the magnitude of the current density, and the yellow thick tube indicates the magnetic flux rope's axis.

diffusivity during the early stages of the eruption. During this extra time, the flux rope quasi-statically raises a little further up, eventually leading to a slight overestimation of the critical value of the decay index.

For one selected run ("Run C") we performed some relaxation runs without increasing the coronal diffusive coefficients. The left panel of Figure 7 shows the current distribution and the decay index along a vertical line passing through the $[\bar{x}, \bar{y}]$ location of the apex. In the "low" diffusion regime the deflected eruption begins at $t_1 = 184t_A$. At this time the apex of the flux rope is at $z \simeq 1.75$. The configuration of the system around the moment of the eruption is shown in the middle and right panels of Figure 7. The semitransparent green plane indicates the height $z = 1.75$ where the decay index at the apex of the magnetic flux rope is $n \simeq 1.4$ (see Figure 7). If the photospheric motions are stopped at $t^* = 180t_A$, no eruption occurs. However, if we stop the flows four Alvén times later, a deflected eruption occurs. At time $t^* = 184t_A$, the axis of the flux rope has just reached the height where $n_{crit} \simeq 1.4$, suggesting that this is the critical decay index in the "low" diffusion regime. Therefore, the critical values of the decay index presented in the previous section should be considered as an upper limit, with a margin of about 7%.

5. DISCUSSION AND CONCLUSION

We perform a series of numerical MHD simulations in order to investigate the initiation and early evolution of flux rope eruptions. We examine how the initiation process depends on the photospheric magnetic field distribution and the current profile of the flux rope. In particular, we examine whether the trigger of the eruption is independent of the boundary flows that drive the system and form the flux rope.

We perform four calculations using different photospheric driving flows. Each calculation is split into three phases characterized by the nature of the applied photospheric driver. In the first two phases, driving flows are imposed in order to form a flux rope. In the final phase, no driver is imposed, and the system is allowed to evolve on its own.

In the first phase, we impose vortex motions (the same for all the calculations) around the isocontours of the normal component of the magnetic field. This flow profile generates electric currents in the volume and causes the system to evolve into a quasi force-free state. At the end of this phase, the

magnetic field consists of a strongly sheared arcade near the PIL enclosed by an overlying quasi-potential field. The flow profile in this phase is chosen to build up shear in the system, not to mimic flows observed on the Sun. Although vortex motions are quite often observed around sunspots, they are rarely so uniform and long lasting (in terms of Alfvén times) as the ones that we impose.

In the second phase, we impose four different classes of photospheric motions. Unlike the previous phase, each of the four calculations is subjected to a different flow profile. The profiles are chosen to mimic different processes commonly observed during the evolution of active regions, such as the deformation and spreading of photospheric magnetic field polarities. Similarly to what is observed on the Sun, these motions have a converging component, i.e., they tend to draw flux toward the PIL. The flows are defined in terms of the magnetic field gradient (see Section 2.2 for details). Since the magnetic field at the boundary is evolved with the induction equation using the line-tied boundary conditions, the flows are nonlinear in both time and space. Finally, all the imposed motions are always sub-Alfvénic (peaking at 5% of the mean coronal Aflvén speed), and the corona responds quasi-statically.

The flows at the photosphere draw flux toward the PIL, where flux cancellation occurs because the magnetic diffusivity in our model is finite. As a consequence, the topology of the magnetic field changes from that of a sheared arcade to that of a configuration with a bald-patch separatrix. During this phase, the applied photospheric flows transport magnetic flux toward a three-dimensional current sheet, which results in the formation of a flux rope through magnetic reconnection at the bald patch. As this process continues, the flux rope slowly rises owing to the buildup of magnetic pressure. However, after a certain point, the system undergoes a transition to a dynamical regime characterized by the exponential growth of the kinetic energy, and the flux rope erupts.

The third phase begins when the rope becomes unstable, at which point we stop all photospheric driving. The instability point is a priori unknown, and we determine it by a series of relaxation runs (see Section 4.1).

In summary, for a complete calculation, we drive the system to form a flux rope, which we then bring to the threshold of instability. At this point we stop driving the system and let it evolve freely to an eruption.

We study the evolution of the system in the framework of the torus instability scenario, because it gives a well-defined threshold that can also be applied to observations. For quasi-statically evolving magnetic fields, it has been shown that the catastrophe and torus instability scenarios give the same prediction for the onset of the loss of equilibrium or the torus instability (Démoulin & Aulanier 2010; Kliem et al. 2014). The same is true when the torus instability criterion is compared with analysis based on the energy of the semi-open field associated with a given magnetic field distribution at the boundary (Amari et al. 2014).

The height of the flux rope when it erupts depends on how the photospheric magnetic field is evolved. Two interesting examples are "Run D1" and "Run D2." For these two calculations the apex of the magnetic flux rope at the onset of the eruption is located at $z \simeq 2.45$ and $z \simeq 1.95$, respectively. Török & Kliem (2007) have shown that the height of the onset of the eruption increases when the distance between the photospheric charges increases. As can be deduced from Figure 1, the central part of the flux distribution for "Run D1" is essentially unmodified, resulting in a highly concentrated flux distribution in the central part of the polarity. However, for "Run D2," the magnetic flux is more uniformly distributed within the whole polarity. As a result, the baricentrum of the magnetic flux is closer to the PIL for "Run D2" than for "Run D1," which results in a dipole with a smaller length scale and, therefore, a lower critical height for the onset of the torus instability.

The top panel of Figure 8 shows the profile of $\alpha = \boldsymbol{J} \cdot \boldsymbol{B}/B^2$ along a vertical line passing through the apex of the axis of the magnetic flux rope at the moment of the onset of the instability. Two different critical heights can be seen in the figure. "Run C" and "Run D2" both have a critical height of $z \simeq 2$, while "Run S" and "Run D1" both have a critical height of $z \simeq 2.4$. The bottom panel of Figure 8 shows the same α profiles, but shifted by the height of the axis of the magnetic flux rope. This allows a direct comparison of the different curves. All the flux ropes are quite similar, but "Run D1" displays some minor differences. A comparison between "Run C," "Run S," and "Run D2" shows that similar flux ropes have different critical heights. In addition, "Run D1" and "Run S" have similar critical heights ($z \simeq 2.4$), but their α profiles are different (within the limitations of a 1D plot). We find that what is crucial for the onset of the eruption is not the actual height of the flux rope, but the fact that the flux rope approaches the regions where the decay index is close to the predicted critical range $n_{\mathrm{crit}} = 1.4$–1.5. This provides strong evidence in favor of the torus instability scenario.

In a current-wire treatment of the torus instability, the morphology of the current channel influences the critical value of the decay index. For example, the critical decay index of a straight wire is typically smaller than a circular wire. For our simulations, we find that the only case with a noteworthy difference in the critical decay index is "Run D2," but its flux rope current profile is not significantly different from those of "Run C" and "Run S." We stress that our model flux ropes are quite similar (see Figure 6); however, it is possible that a geometrical effect may have also played a role in the eruption, although it cannot be easily disentangled in our asymmetric configuration. Nevertheless, it is interesting that "Run D2" is the case that displays a lower value of the critical decay index and is also the one where the convergence flows induce the
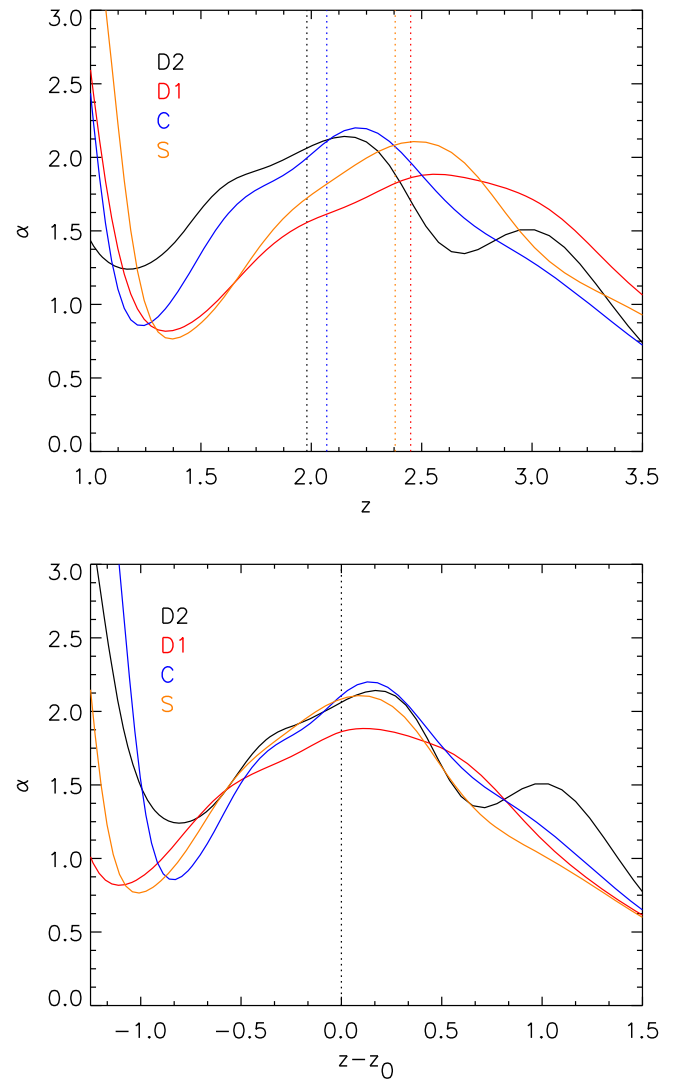

Figure 8. Top panel: vertical dependence of $\alpha = \boldsymbol{J} \cdot \boldsymbol{B}/B^2$ along a line passing through the magnetic flux rope's axis. The vertical dotted lines indicate the height of the magnetic flux rope's apex for each simulation (color code) at the moment of the onset of the instability. Bottom panel: same as the top panel, but now the plot is shifted along the z-axis by an amount z_0, equal to the height of the axis of the magnetic flux ropes.

most significant modification of B_z at the boundary. The lower values of the critical decay index in the latter simulation may be due to the different evolution of the bald-patch separatrix, which possibly induces different line-tying effects.

Figure 6 shows a local enhancement in the current density in the whole volume of the flux rope. This suggests that if one wanted to compare our flux rope model with the wire models, one should consider an almost circular, relatively thick current channel. In this context, Démoulin & Aulanier (2010) predicted a critical value of the decay index that depends on whether or not the current channel expands during the perturbation. The value that we find, $n_{\mathrm{crit}} \simeq 1.4$–$1.5$, would be compatible with a flux rope that has constant current during the perturbation. However, the simulation without the "increased" diffusion showed that this range could be up to about 7% lower, that is, $n_{\mathrm{crit}} \simeq 1.3$–$1.4$. This range would also be compatible with circular current wires with a time-varying current. Various processes can influence the evolution of the current within the flux rope as it evolves. During its slow quasi-static rise, the flux
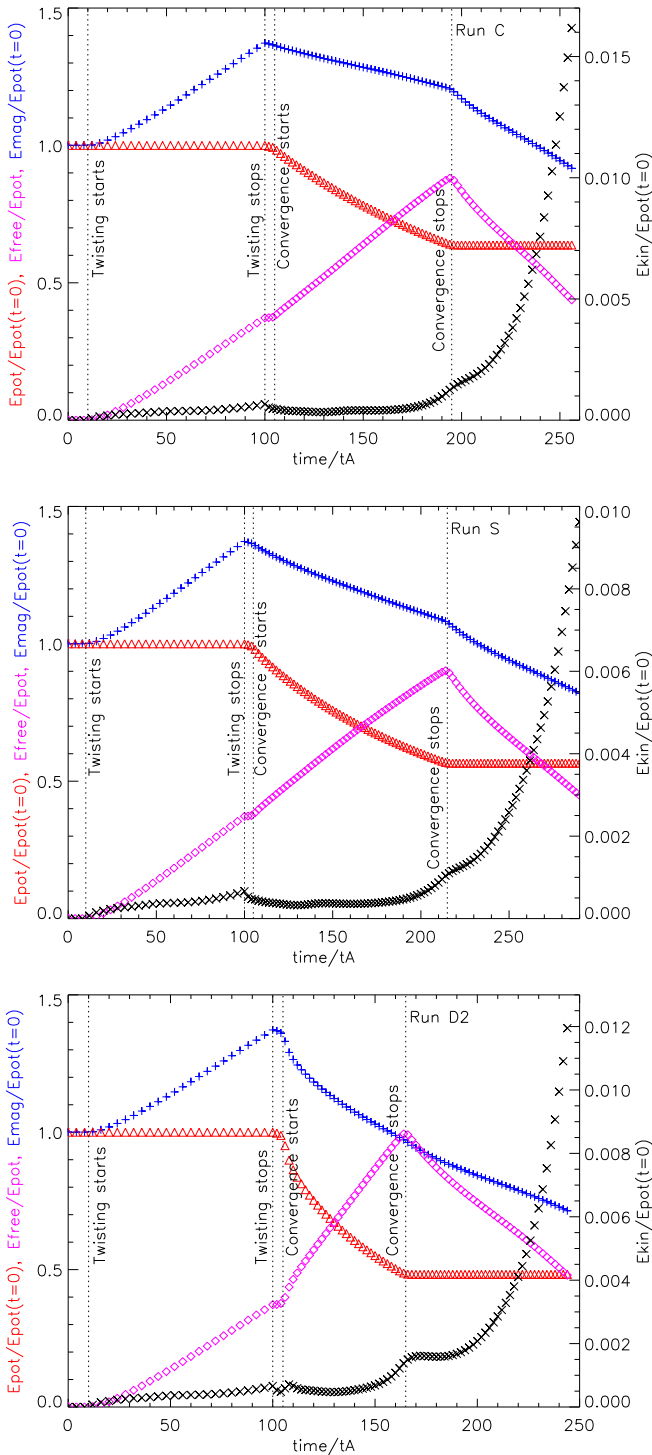
Figure 9. Temporal evolution of the free magnetic energy in the system (purple "◇") as well as of the kinetic (black "×"), potential (red "△") and total (blue "+") magnetic energy of the system normalized to the energy of the initial (potential) magnetic field for "Run C," "Run S" and "Run D2" (from top-left to bottom-right, respectively). The magnetic energy of the initial potential field is $E_{pot}(t=0) = 174.4$.

rope expands, which causes its twist per unit length to decrease. As a result, the volume current in the rope also decreases. However, during the formation process, and subsequently the eruption itself, magnetic reconnection at the bald patch, and subsequently at the flare current sheet, clearly injects some sheared, current-carrying, magnetic flux into the flux rope, and

this must eventually increase the volume current therein. If the two opposite effects balance each other, then the volume current of the flux rope may not vary too much, which will result in an instability threshold similar to the one for currents rings with a modest temporal variation of the current, that is, $n_{crit} \in [1.2 - 1.5]$ (Démoulin & Aulanier 2010).

The analysis presented in this paper suggests that the trigger of the eruptions is the torus instability regardless of the exact morphology of the magnetic flux rope and of the photospheric evolution of the active region. However, several phenomena, such as line-tying, magnetic reconnection at bald patches, and different evolution of the photospheric magnetic field, affect the critical decay index for the onset of the instability, resulting in a "critical range" rather than a "critical value." We speculate that the decrease of the current due to the flux rope expansion and its increase due to the bald-patch reconnection compensate, resulting in a critical range that is not too different from the analytical predictions of the wire models.

APPENDIX

In Section 3.2 and Figure 3 we presented the evolution of the potential, free, and total magnetic energies, as well as the kinetic energy for "Run D1." In Figure 9 we report the same plots for the other simulation runs.

REFERENCES

Alissandrakis, C. E. 1981, A&A, 100, 197
Amari, T., Canou, A., & Aly, J.-J. 2014, Natur, 514, 465
An, J. M., & Magara, T. 2013, ApJ, 773, 21
Aulanier, G. 2014, in IAU Symp. 300, Nature of Prominences and their Role in Space Weather, ed. B. Schmieder, J.-M. Malherbe, & S. T. Wu (Cambridge: Cambridge Univ. Press), 184
Aulanier, G., & Demoulin, P. 1998, A&A, 329, 1125
Aulanier, G., Démoulin, P., & Grappin, R. 2005, A&A, 430, 1067
Aulanier, G., Janvier, M., & Schmieder, B. 2012, A&A, 543, A110
Aulanier, G., Török, T., Démoulin, P., & DeLuca, E. E. 2010, ApJ, 708, 314
Bateman, G. 1978, MHD Instabilities (Cambridge: MIT Press)
Canou, A., & Amari, T. 2010, ApJ, 715, 1566
Chandra, R., Dagum, L., Kohr, D., et al. 2001, Parallel Programming in OpenMP (San Francisco, CA: Morgan Kaufmann Publishers)
Chen, P. F. 2011, LRSP, 8
Démoulin, P., & Aulanier, G. 2010, ApJ, 718, 1388
Demoulin, P., & Priest, E. R. 1989, A&A, 214, 360
Fan, Y. 2010, ApJ, 719, 728
Fan, Y., & Gibson, S. E. 2007, ApJ, 668, 1232
Filippov, B., Martsenyuk, O., Srivastava, A. K., & Uddin, W. 2015, JApA
Forbes, T. 2010, in Models of Coronal Mass Ejections and Flares, ed. C. J. Schrijver & G. L. Siscoe (Cambridge: Cambridge Univ. Press), 159
Forbes, T. G., & Isenberg, P. A. 1991, ApJ, 373, 294
Forbes, T. G., Linker, J. A., Chen, J., et al. 2006, SSRv, 123, 251
Gibb, G. P. S., Mackay, D. H., Green, L. M., & Meyer, K. A. 2014, ApJ, 782, 71
Gibson, S. E., Kucera, T. A., Rastawicki, D., et al. 2010, ApJ, 724, 1133
Green, L. M., Kliem, B., & Wallace, A. J. 2011, A&A, 526, A2

Gropp, W., Lusk, E., & Skjellum, A. 1999, Using MPI: Portable Parallel Programming with the Message-passing Interface (2nd ed.; Cambridge, MA: MIT Press)

Gunár, S., & Mackay, D. H. 2015, ApJ, 803, 64

Inoue, S., Hayashi, K., Magara, T., Choe, G. S., & Park, Y. D. 2015, ApJ, 803, 73

Isenberg, P. A., Forbes, T. G., & Demoulin, P. 1993, ApJ, 417, 368

Jiang, C., Wu, S. T., Feng, X., & Hu, Q. 2014, ApJL, 786, L16

Jing, J., Yuan, Y., Wiegelmann, T., et al. 2010, ApJL, 719, L56

Kliem, B., Lin, J., Forbes, T. G., Priest, E. R., & Török, T. 2014, ApJ, 789, 46

Kliem, B., Su, Y. N., van Ballegooijen, A. A., & DeLuca, E. E. 2013, ApJ, 779, 129

Kliem, B., & Török, T. 2006, PhRvL, 96, 255002

Kuperus, M., & Raadu, M. A. 1974, A&A, 31, 189

Lin, J., & Forbes, T. G. 2000, JGR, 105, 2375

Mackay, D. H., & van Ballegooijen, A. A. 2006, ApJ, 641, 577

Olmedo, O., & Zhang, J. 2010, ApJ, 718, 433

Priest, E. R., Hood, A. W., & Anzer, U. 1989, ApJ, 344, 1010

Rachmeler, L. A., Gibson, S. E., Dove, J. B., DeVore, C. R., & Fan, Y. 2013, SoPh, 288, 617

Savcheva, A. S., Green, L. M., van Ballegooijen, A. A., & DeLuca, E. E. 2012, ApJ, 759, 105

Titov, V. S., & Démoulin, P. 1999, A&A, 351, 707

Török, T., & Kliem, B. 2005, ApJL, 630, L97

Török, T., & Kliem, B. 2007, AN, 328, 743

van Ballegooijen, A. A. 2004, ApJ, 612, 519

van Ballegooijen, A. A., & Martens, P. C. H. 1989, ApJ, 343, 971

Zuccarello, F. P., Meliani, Z., & Poedts, S. 2012, ApJ, 758, 117